

The Mesoscale Crystallinity of Nacreous Pearls

Jiseok Gim

University of Michigan-Ann Arbor <https://orcid.org/0000-0001-7499-873X>

Alden Koch

University of Michigan

Laura Otter

The Australian National University <https://orcid.org/0000-0003-0737-4497>

Benjamin Savitzky

Cornell University

Sveinung Erland

Western Norway University of Applied Sciences <https://orcid.org/0000-0003-0175-8801>

Lara Estroff

Cornell University <https://orcid.org/0000-0002-7658-1265>

Dorrit Jacob

The Australian National University

Robert Hovden (✉ hovden@umich.edu)

University of Michigan <https://orcid.org/0000-0002-3403-8803>

Article

Keywords: pearls, nacre, crystallinity

Posted Date: March 11th, 2021

DOI: <https://doi.org/10.21203/rs.3.rs-278534/v1>

License:  This work is licensed under a Creative Commons Attribution 4.0 International License.

[Read Full License](#)

The Mesoscale Crystallinity of Nacreous Pearls

Jiseok Gim¹, Alden Koch², Laura M. Otter³, Benjamin H. Savitzky⁴, Sveinung Erland⁵, Lara A. Estroff⁶, Dorrit E. Jacob³, Robert Hovden^{1,7*}

¹. Department of Materials Science & Engineering, University of Michigan, Ann Arbor, MI, USA

². Department of Biomedical Engineering, University of Michigan, Ann Arbor, MI, USA

³. Research School of Earth Sciences, Australian National University, Canberra, ACT 2600, Australia

⁴. National Center for Electron Microscopy, Molecular Foundry, Lawrence Berkeley National Laboratory, Berkeley, CA, USA

⁵. Department of Maritime Studies, Western Norway University of Applied Sciences, Haugesund, Norway

⁶. Department of Materials Science & Engineering, Cornell University, Ithaca, NY, United States

⁷. Applied Physics Program, University of Michigan, Ann Arbor, MI, USA

*Correspondence and requests for materials should be addressed to R.H. (email: hovden@umich.edu).

A pearl's distinguished beauty and toughness is attributable to the periodic stacking of aragonite tablets known as nacre. Nacre is a naturally occurring mesocrystal that remarkably arises in the absence of translational symmetry. Gleaning the inspiring biomimetic design of a pearl requires quantifying its structural coherence and understanding the stochastic processes that govern formation. By characterizing the entire structure of pearls (~3 mm) in cross-section at high resolution, we show nacre is a medium-range mesocrystal formed through nanoparticle assembly processes. Self-correcting growth mechanisms actively remedy disorder and topological defects of the tablets and act as a countervailing force to paracrystallinity (i.e. long-range disorder). Nacre has a correlation length of roughly 16 tablets (~5.5 μm) despite persistent fluctuations and topological defects. For longer distances (> 25 tablets, ~8.5 μm), the frequency spectrum of nacre tablets follows $f^{-1.5}$ behavior suggesting growth is coupled to external stochastic processes—a universality found across disparate natural phenomena which now includes pearls.

Introduction

The artist Jorge Méndez Blake illustrated a basic principle of structure in mesocrystals and grown nanocrystalline materials when he placed a single book (i.e. a defect) in a brick wall, displacing every subsequent brick layer¹. Blake's work demonstrates the principle of paracrystallinity: disorder from any one defective site propagates throughout the layers of the material²⁻⁴. In the context of brick-laying, skilled masons overcome this difficulty using external templates to achieve translational order—marked guideposts and lacing cords align layers to prevent disorder from propagating^{5,6}. Only with great calculated effort can a ten-story building ensure the same number of aligned brick layers on all sides⁷. Regarding layered growth of nanomaterials, of course, external templates do not exist. Mesocrystallinity—long range translational order of mesoscopic building blocks—is thus improbable due to natural variations in the unit sizes, without the aid of some additional countervailing mechanism. The rare instances where nature assembles mesocrystals therefore merits our attention⁸. Nacre in pearls and mollusk shells are one such example where mesocrystallinity arises in an environment absent of translational symmetry⁹⁻¹¹.

Pearls are renowned and coveted for their beauty; that beauty results from the diffracting iridescence of periodically stacked tablets (~500 nm thick units) known as nacre¹²⁻¹⁵. Nacre is grown layer-by-layer, with aragonitic tablets bonded by soft interlamellar organic layers (~10-20 nm thickness). These tablets define the unit cell of a mesocrystal. The mesocrystal is a highly ductile structural composite that can withstand mechanical impact and exhibits high resilience on the macro- and nano-scale¹⁶⁻¹⁸. Because of its superior toughness, nacreous shells protect the mollusk's soft body^{10,19-21}, which inspires scientists designing next-generation super-composites²²⁻²⁴. Yet, despite a century of scientific fascination with nacre^{9,10,17,19,25}, its astonishing mesoscale crystallinity has not been quantified, leaving key questions about this material unanswered: does nacre have long-range order? What is the stochastic process that govern its formation?

Here we show nacre is a remarkable medium-range mesocrystal formed through corrective processes that remedy disorder and topological defects. The entire nanostructure of nacreous pearls is characterized in cross-section to reveal complex stochastic processes that govern ordered nacre growth. Beginning atop an initially formed organic center, nanocrystallites self-assemble into bulk aragonite that becomes a substrate to nacre. The initial layers of nacre laid over this substrate are disordered; however, this disorder attenuates within the first 200 layers through self-corrective

growth processes that persist throughout the entire pearl. When a tablet is grown too thin, the next tends to be thicker—and vice versa—thus compensating for the initial error. Local irregularities in thickness ($\pm 15^\circ$ variation of interfacial curvature) and topological defects ($5.9 \times 10^8 \text{ m}^{-2}$ defect density) intermittently appear, yet the pearl maintains order with a correlation length of ~ 16 tablets ($\sim 5.5 \mu\text{m}$). However, a pearl is not a perfect mesocrystal and local disorder persists into subsequent layers—a paracrystalline property which ultimately limits long-range order. For longer length-scales (e.g., > 25 tablets. $\sim 8.5 \mu\text{m}$) the aperiodic fluctuation of nacre's tablet thicknesses follow $f^{-1.5}$ noise behavior, which represents external Markov processes with longer memory attributable to cooperative environmental changes such as temperature, pH, food availability, seasonality, and tidal cycles.

Results

The Start of Nacre in Pearl. Pearls form either as a natural response to mantle tissue injury or when mantle tissue is deliberately transplanted from a donor into a host shell for pearl culturing. In both cases, the mantle epithelium develops a closed cyst—the so-called pearl sac—programmed to reproduce the structure of the shell²⁶. CaCO_3 is then secreted onto a manufactured bead (for bead-cultured pearls) or any available debris enclosed by the developing pearl-sac (for non-beaded pearls) within a limited space²⁷. The shape of the manufactured or natural nucleus usually dictates a pearl's macroscopic shape^{27,28} (Supplemental Fig 1-5). Here we primarily study non-bead-cultured “keshi” pearls, grown for ca. 18 months in *Pinctada imbricata fucata* mollusks on the Eastern shoreline of Australia (see Methods)²⁹.

The cross section of a non-bead “keshi” pearl is shown in Figure 1b. The mollusk deposits calcium carbonate upon the irregular organic center ($\sim 400 \mu\text{m}$ diameter) and after roughly $\sim 15 \mu\text{m}$ of bulk aragonite, nacre layers begin to form. Nacre layers are bonded by chitin membranes periodically and synchronously deposited by the epithelium^{30,31}. Ordered nacre makes up 87% of this 2.5 mm pearl (Fig. 1b,c). However, the nacre is preceded by more disordered growth stages. Nacre and other biominerals form by non-classical crystallization via metastable transient precursor phases^{32,33} and oriented attachment of CaCO_3 nanoparticles orchestrated by organic macromolecules (Fig. 1g,h, Supplemental Fig. 6). The nanoparticles are aragonite crystals in their final form (Supplemental Fig. 7) and their packing intermittently increases until forming columnar aragonite with segregated regions of organic. In Fig. 1b this occurs over roughly $200 \mu\text{m}$ of growth.

Throughout this process, the pearl's volume becomes larger and rounder, before penultimately forming a bulk aragonite (Fig. 1c). In most observations, we observe bulk aragonite begins after a region reaches positive curvature³⁴⁻³⁶.

In pearls, nacre forms abruptly on bulk aragonite. At the start of nacre, around 440 μm ($\pm 12\%$) from the organic center in Figure 1, the bulk aragonite is an approximately flat substrate (curvature of ~ 0.002) with locally rough texture ($\sim 200 \text{ nm}$ variation over $7 \mu\text{m}$). About 10-20 μm prior to the first nacre layer, the bulk organic phases show deposits equal to the amount observed for mature nacre suggesting the genetic processes directing the system towards nacre deposition start earlier than the structure itself (Supplemental Fig. 9). The same transition was found in non-bead cultured Tahitian “keshi” pearls produced by the *Pinctada margaritifera* mollusk (Supplemental Fig. 8). This direct nacre growth onto bulk aragonite in pearls is distinct from nacre formation reported in mollusk shells (e.g. *Pinna nobilis*) where the assembly process is driven by aggregation of nanoparticles within a several-micron-thick organic matrix³⁷.

Mesocrystallinity of Nacre. The first nacre tablets are non-uniform with substantial thickness variation due to the rough aragonitic substrate on which it forms. The Fourier transform of early nacre layers imaged by annular dark-field scanning transmission electron microscopy (ADF-STEM) reveals $\pm 15^\circ$ angular variation in their interface curvature (Inset of Fig. 2a). This angular broadening decreases quickly to $\pm 6^\circ$ after 100 layers and further down to $\pm 5^\circ$ after 200 layers (mature nacre). This smoothing of tablet interfaces is clearly visible (Fig. 2a, Supplementary Fig. 10). At the same time, tablet thickness decreases by 30%, reducing from $500 \pm 300 \text{ nm}$ for early-nacre to $340 \pm 120 \text{ nm}$ (a $\sim 40\%$ reduction of variance) for mature nacre. In mature nacre (Fig. 2a) peaks visible in the Fourier transform provide the signature presence of mesocrystallinity. However, these peaks in Fourier space do not quantify the long-range order nor describe the stochastic processes that create the mesocrystal.

Pair-correlation functions quantify the mesocrystallinity of nacre in pearls along the growth direction (Fig. 2b) by measuring the probability of tablet spacings (see Methods). Subsequent peaks indicate the distance to the 1st nearest neighbor (NN), 2nd NN, 3rd NN, and etc. These plots were calculated based on all pairs of tablets in each stage of nacre (Fig. 2a). The first peak represents the average distance between adjacent tablets and subsequent peaks describe longer-

range order in the crystal. For ideal crystals, every peak will appear equally sharp. However, in nacre, peaks in the pair-correlation function increasingly broaden—indicating propagation of disorder, as described by the paracrystal model^{4,38,39}.

Nacre is well described as an ordered paracrystal or medium-ranged mesocrystal. We report mature nacre has a correlation length of 5.5 μm and translational order is lost by 16 layers. Correlation length is defined as the length where the pair-correlation envelope disappears. (See Methods and Supplementary Fig. 11). Thus, although nacre maintains extraordinary translational symmetry across a dozen or so layers, it lacks the long-range order of a true mesocrystal. In paracrystals, a deviation in layer thickness displaces subsequent layers and thus disorder propagates. Defects and tablet variation degrade translational symmetry with distance. The progressive broadening of each peak in the pair-correlation functions quantifies the long-range order and paracrystallinity (Fig. 2d). In a perfect paracrystal, the standard deviation of peaks broadens by the square root of its peak number ($\sigma_n = \sigma_1 \sqrt{n}$)^{4,40}.

Nacre shares crystalline and paracrystalline structure. As shown in Figure 2d, nacre falls below the paracrystal curve (more ordered) and above the flat crystalline curve. The paracrystallinity, or broadening of peaks, is approximately equivalent in early, mid, and mature-stage nacre suggesting the growth mechanisms may be equivalent. However, the sharper first order peaks in mature nacre reflect improved initial conditions (i.e., early nacre begins on a rough substrate).

Nacre maintains crystallinity through self-correcting growth processes. Each nacre layer attenuates the bumps and valleys of the previous nacre layer. If one tablet is thicker than average, the next tends to be thinner. This negative correlation of thickness between adjacent nacre layers is quantified in the early, mid, and mature nacre in Figure 2c. The negative correlation is strong and follows an autoregressive model that allows ordered mesocrystalline growth to reach steady state in ~200 layers, which demarcates maturity. In uncorrelated growth, thickness variation of each nacre tablet would devastate the long-range order of the mesocrystal—much like Jorge Méndez Blake’s brick wall¹. However, nacre self-corrects for fluctuations in tablet thicknesses and occasional screw dislocations (Fig. 3a,b, Supplementary Fig. 12,13).

Topological Defects in Nacre. Local disorder in pearls encompasses topological defects (i.e., screw dislocations) of the tablets and organic interfaces. SEM images at the pearl surface and a

corresponding schematic illustrates how screw dislocations originate in nacre (Fig. 3a,b, Supplementary Fig. 12,13). High-resolution ADF-STEM images show the dislocation in cross-section along perpendicular axis (Fig. 3c-l, Supplementary Fig. 13). When viewed parallel to the slip plane, a mineral bridge at the dislocation marks the defect origin. Viewed normal to the slip plane the screw dislocation appears as an additional, partial organic boundary. Screw dislocations in nacre are known⁴¹⁻⁴³ and recently reported to couple as chiral pairs through a dissipative distortion field that helps accommodate the space filling requirements of nacre²⁵. In cross sections, screw dislocations can be easily mis-identified as edge dislocations. The defect density of nacreous pearls herein is $5.3 \pm 0.4 \times 10^8 \text{ m}^{-2}$ in plane-view and $6.5 \pm 0.4 \times 10^8 \text{ m}^{-2}$ in cross-section (Fig. 3a, Supplementary Fig. 14)—this approximate equivalence suggests a homogeneous screw dislocation distribution in three-dimensions. The dislocation density of nacre is comparable to typical engineering ceramic materials' defect density of around $10^8\text{--}10^{10} \text{ m}^{-2}$ ⁴³⁻⁴⁵. Our quantification is measured from top-view and cross-sectional SEM by dividing the total number of defects by the total area (Supplementary Fig. 14).

Despite the prevalence of screw dislocations, nacre's self-correcting growth processes preserve mesocrystallinity via substantial thickness changes (~28%) at the topological singularity. Figure 3f,g,k,l shows tablet thicknesses at and around screw dislocations viewed in cross section parallel or perpendicular to the slip plane. The singularity causes tablets to become thinner to accommodate an additional layer without disrupting the long-range order of the mesocrystal. Within just a couple layers, above or below the dislocation, nacre visually returns to uniform, periodic growth.

Stochastic Nacre Growth Follows 1/f Behavior. To understand the stochastic growth processes over longer lengths and time, nacre tablet thicknesses are analyzed across the entire pearl (2.5 mm diameter) at high-resolution (~3 nm) (Fig. 4a). This pearl contained 2615 tablet layers deposited over 548 days giving a mean growth rate of 4 to 5 tablets (1.4 -1.7 μm) per day—in this regard distances may also be considered in terms of time (see Methods). Every tablet of nacre is measured from a mosaic of back-scattered SEM images and a profile of their thicknesses is plotted in chronological order in Figure 4c. Initial thicknesses fluctuate substantially but reduce quickly within ~10 layers (Fig. 4c, yellow box), as shown in the thickness map (Fig. 4d). Notably, sawtooth-shaped bursts in systematic thickness variation are visible (Fig. 4c, red box) and repeat aperiodically throughout the entire growth (Fig. 4e). The stochastic processes of nacre growth are

revealed in a power spectral density (i.e., squared magnitude of the Fourier transform) of the thickness profile (Figure 4b). The spectral density shows two distinct regimes: power law decay across a low to mid frequency regime corresponding to timescales greater than ~5-6 days or distances longer than ~25 tablets and a high frequency regime where the density slightly increases.

The spectral density of a pearl's tablet thicknesses follows power-law decay across low to mid frequencies, colloquially called 1/f noise, suggesting nacre growth has correlations that extend over a wide range of timescales with cooperative effects linked to environmental changes. In stochastic Markov processes the distribution of future events are determined by recent past events,^{46,47} and even simple Markov processes can exhibit a spectral density following $f^{-\alpha}$ where $1 < \alpha < 2$. This behavior characterizes a wide range of phenomena from fluctuations in river flow to heart-beats or economic markets^{48,49}. The spectral density of nacre follows $f^{-1.5}$ across low to mid frequencies ($>\sim 25$ tablets or $>\sim 6$ days). In real-space this corresponds to the saw-tooth shaped bursts in the thickness profile of Fig. 4c,e. Such aperiodic fluctuations can be associated with the $f^{-1.5}$ spectral density and the behavior can be explained by the additive effect of one or several Markov processes representing the external effect of environmental and physiological factors. The coefficient α of power-law decay is estimated by truncating the PSD and applying a square fit for log-log coordinates (See Methods).

The observed power law decay, $f^{-1.5}$, suggests that nacre's growth is governed by a set of stochastic processes with different characteristic time scales. This makes sense: we expect growth to depend on many external factors in the surrounding habitat of the mollusk shell¹³⁻¹⁵. Multiple clocks in nature govern these living animals such as the 30-day circalunar cycle^{50,51}, the day-night circadian cycle^{52,53}, tidal changes⁵⁴, hibernation in the winter^{55,56}, and aestivation in the summer^{57,58}. This fluctuating marine environment and the natural time scales of the mollusk are interconnected influences of the non-equilibrium thermodynamical conditions⁵⁹⁻⁶¹ of nacre growth and likely explains the observed power law behavior.

At high frequencies ($< \sim 25$ tablets or $\sim 4-5$ days), there is a flattening of the 1/f noise and a slight increase in the power spectrum due to corrective growth processes whereby the thickness of each tablet is anticorrelated with the thickness of the previous layer. The opposing fluctuations in subsequent layers (shown in Fig. 2c) amplifies high frequency variations in a manner consistent

with a negative autoregressive process⁶²⁻⁶⁴ and causes the slightly increasing profile of the spectral density at high frequencies (Fig. 4b). Mechanistically, the source of this correlative correction is not clear—it may be explained by a partial viscosity of the CaCO₃ upon deposition under isostatic pressure or possibly by physiological responses.

In nacre, we see a fundamental tradeoff between achieving mesocrystallinity and minimizing tablet thickness variation. Corrective growth occurs to counterbalance disorder and the natural tendency towards paracrystallinity thereby enabling surprising and remarkable mesocrystalline ordering. However, this corrective growth process amplifies variation wherein perturbations in one layer causes an opposite perturbation in subsequent layers.

Discussion

Pearls are iconic mesoscale crystal grown by mollusks with no external templates along the direction of growth. Nanoparticles assemble within an organic matrix with increasing density until a rough massive, structurally indistinct aragonite forms and later serves as substrate for nacre deposition. Tablets are then grown layer-by-layer with self-correcting mechanisms that allow the mesocrystal to accommodate tablet variation and topological defects. Mollusks strike balance between preserving translational symmetry and reducing thickness variation by creating a paracrystal with medium-range order (~5.5 μm coherence length). This balance allows pearls to attenuate the initial disorder during early formation and maintain order throughout a changing external environment. Over longer timescales (>~6 days), nacre growth is mediated by external stochastic processes and exhibits a ‘1/f’ behavior that belongs to a universal class of vast and disparate phenomena. Quantifying the mesocrystallinity of nacreous pearls reveals underlying processes of formation and provides new metrics and illuminates new paths toward mimicking nacre’s hierarchical design.

Methods

Specimen. Specimens of nacreous non-bead cultured Akoya “keshi” pearls produced by the *Pinctada imbricata fucata* pearl-oyster were collected at the Broken Bay Pearl farm (Pearls of Australia Pty Ltd) located on the East coast of Australia. The term keshi pearls is used today to describe beadless pearls that were unintentionally produced as a byproduct of culturing bead-cultured pearls⁶⁵. This farm was chosen as

it avoids post-harvest treatments such as bleaching or dying as is otherwise common practice²⁹ (Otter et al., 2017).

Wedge-polishing preparation. Cross-sections were cut from the whole pearls measuring 3-5 mm in diameter using a diamond wire saw. The cross-sections for S/TEM were prepared by mechanical wedge polishing^{10,17}, which provides large-area, electron-transparent specimens with structural stability.

Electron microscopy. SEM images were recorded with a Z-contrast backscattered electron detector of a JEOL IT500 system (10 kV) with an XEDS (X-ray Energy Dispersive Spectroscopy) detector. High angle annular dark-field scanning transmission electron microscopy (ADF-STEM) were performed using a JEOL 3100R05 microscope with Cs aberration corrected STEM (300 keV, 15 mrad) and cold field emission gun. A ADF detector with 120–150 mm camera lengths and a detector angle of 59~74 (inner) – 354~443 mrad (outer) were used to produce Z-contrast images where greyscale intensity is sensitive to the atomic number in the specimen’s matrix. Column pressure in the STEM column at the specimen was $\sim 1 \times 10^7$ torr.

Low-dose methods, beam shuttering, and examination of regions exposed to the beam were used to separate electron beam irradiation from intrinsic phenomena^{10,17}. For STEM measurements, with typical fields of view from ~500 nm to 10 μm the electron dose was typically from ~0.4 to 90 $e^- \cdot \text{\AA}^{-2}$ and dose rates ranging from around ~0.1 to 2.7 $e^- \cdot \text{\AA}^{-2} \cdot \text{s}^{-1}$. The material was structurally preserved during imaging. However, for the same imaging conditions at higher magnifications (e.g., 20 nm field of view) the radiation dose increases to $\sim 9 \times 10^5 e^- \cdot \text{\AA}^{-2}$ and dose rate to $\sim 3 \times 10^3 e^- \cdot \text{\AA}^{-2} \cdot \text{s}^{-1}$ which causes the material to show electron irradiation damage localized to the small field of view. Thus, larger fields of view are preferred to minimize dose and provide a large area of observation. Atomic resolution STEM requires a small field of view with an on-axis region of interest.

Relative organic concentration in nacre tablets is determined by the area ratio of visible organic phases to mineral. Based on backscattered electron intensity, the area is assigned by thresholding the range of intensities corresponding to the organic phases. The estimated concentration of organic phases in mature nacre is ~5 vol.% which is within a reasonable range of organic concentrations previously reported⁶⁶ (Supplementary Fig.7).

Nacre’s growth rate is counted backward based on the age of pearl. We assume that only nacre growth takes out most of the Pearl’s lifetime because nacre occupies almost 90% of the entire volume compared to the bulk aragonite and the growth rate of nacre along c-axis is slower than that of the aragonite^{67,68}. Thus, the growth rate of nacre is the total number of nacre layers (e.g. 2615 layers) divided by the lifetime of pearl (e.g. 18 months ~ 548 days).

Raman Spectroscopy. Confocal Raman spectroscopy was performed on the cross-sections of pearls using a Tescan RISE Microscope equipped with a WITec confocal Raman microscope. Raman spectra in the spectral range ($100\text{--}3700\text{ cm}^{-1}$) were recorded with a CCD camera using a solid-state 532 nm laser as the excitation source (spectral grating: 600 g/mm, laser power: 10~15 mW, optical lens: 100x). Each Raman spectrum was acquired typically for 0.5~1 s, and with 30~100 of scans to minimize noise effects. The parameters for excitation power, acquisitions and accumulations are selected to prevent the sample from laser burn. Spectral reproducibility was confirmed by taking several spot analyses.

Data analysis. The pair correlation function describes the probability distributions of nearest-neighbor (NN) tablets in space about a known tablet position³⁹. The one-dimensional pair correlation function is extracted from raw back-scattered electron (BSE) SEM images with high resolution (~3 nm). Mechanical scratches are removed using the image filtering⁶⁹. Interlamellar membranes are identified by finding local minima in BSE intensity line profiles taken perpendicular to the nacre layers. The resulting interfacial positions are then used to calculate the thickness of nacre layers by measuring the distance between positions. The N^{th} tablet thickness is calculated as the difference between the N^{th} and $(N+1)^{\text{th}}$ interface positions. A 1D histogram of tablet thickness was then calculated and normalized by a factor of $\frac{1}{k \cdot bw}$ to obtain a discretization of the pair correlation function, where k is the number of samples and bw is the histogram bin width. A sum of normalized gaussians is fit to the histogram peaks and the standard deviations are plotted vs peak order.

Correlation between the widths of adjacent tablets is calculated by measuring the deviation in tablet width from the local mean tablet width. The local mean is calculated from the list of all sampled tablet widths using a rolling average with a width of three tablets. Thus, the deviation in thickness of the nth tablet is given as $width_N - (width_{(N-1)} + width_N + width_{(N+1)}) / 3$. Deviations in thickness of pairs of adjacent tablets are plotted against each other and the correlation coefficient is estimated by linear least squares fitting. Correlation length is defined as the length where the pair-correlation envelope disappears. It becomes negligible when the magnitude of the following peak is below 10% of the first peak (i.e., $\frac{h_x}{h_1} < 0.1$). Transitional symmetry is lost by 16 layers (i.e., 5.5 μm).

Autocorrelation of tablet's stochastic process can be interpreted by power spectral density (PSD), that is generated in the frequency domain by squaring a fast Fourier Transform of thickness profile. The tablet thickness is measured from BSE SEM images using the peak detection algorithm described above and is plotted in chronological order where the values are evenly spaced. Since the Fourier transform is not a consistent estimator (the variance is not reduced when the number of data points increases), the PSD is

averaged over the profiles from ten neighboring regions and is linearized in log-log scale to reveal 1/f noise. The logarithmic PSD is fitted by polynomial least squares methods to determine the power-law decay coefficient α of the 1/f noise component (i.e., the slope of 1/f noise) for $0.04 < f < 0.0004$ (25 to 2,500 tablets). For frequencies higher than 0.04, the 1/f noise is flattened and change the slope to be positive.

Acknowledgements

The authors acknowledge the University of Michigan College of Engineering for financial support and the Michigan Center for Materials Characterization for use of the instruments. We thank Pearls of Australia Pty Ltd and the Broken Bay Pearl Farm for providing the akoya keshi pearls, and Professor Pupa U. P. A. Gilbert for providing non-bead-cultured Tahiti keshi pearl.

Authors contribution

Sample preparation was developed by J.G.; electron microscopy was conducted by J.G.; optical microscopy was performed by J.G. and A.K.; data analysis and materials interpretation were carried out by J.G., A.K., B.M.S., S.E., and R.H.; biological context was provided by L.M.O., L.A.E., and D.E.J.; all authors discussed the results and commented on the manuscript. J.G., A.K., L.M.O., B.M.S., and R.H. wrote the manuscript.

Competing financial interests: The authors declare no competing financial interests.

Figures:

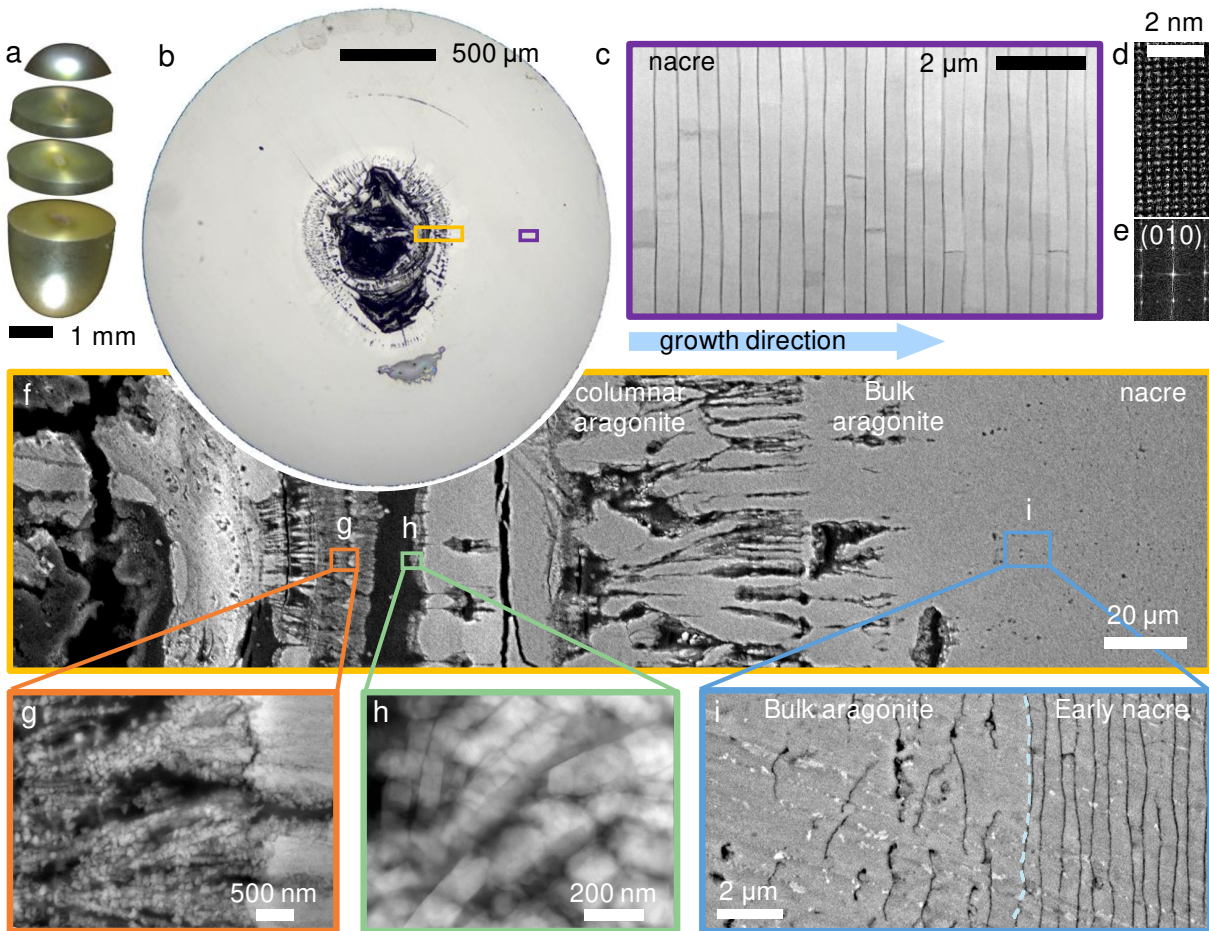


Figure 1 Formation of non-bead-cultured akoya “keshi” pearls produced in a *Pinctada imbricata fucata* mollusk. **a** Optical overview of a non-beaded keshi cultured pearl showing iridescence due to the interplay of constructive interference at nacre tablet layers with light. **b** Cross-section showing CaCO₃ growth begins onto an organic center. **c** Mature nacre (purple box in b) showing ordered state in their thickness and interface curvature. **d,e** Atomic resolution ADF STEM of mature nacre and its corresponding Fourier Transform indicating highly crystalline nacre and a lattice constant that is consistent with aragonite. **f** Cross-sectional backscatter SEM at the center of the pearl (yellow box in b) showing transition from spherulitic aragonite structures to nacre. **g,h** Oriented attachment of nanocrystallites that form massive, structurally indistinct aragonite structure. **i** Formation of nacre begins directly on massive, structurally indistinct aragonite.

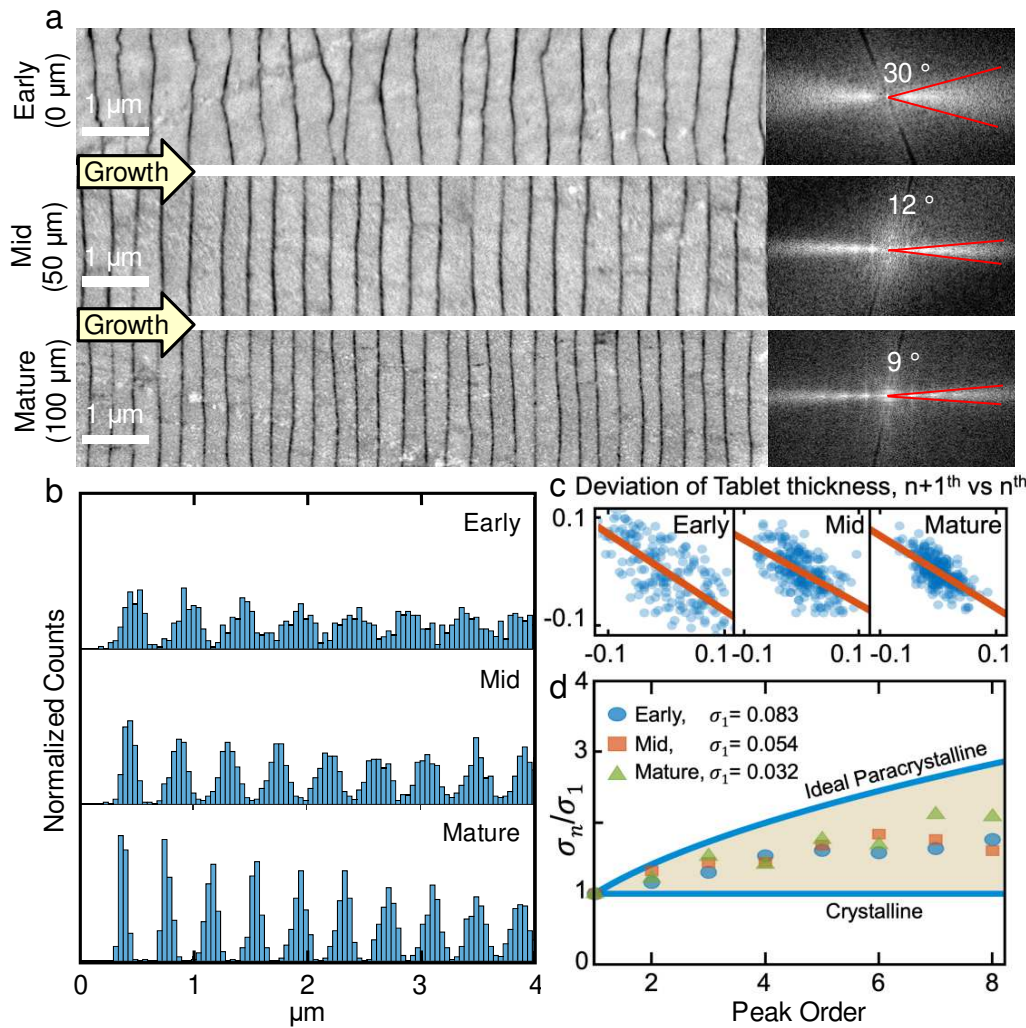


Figure 2 Quantification of mesocrystallinity in nacre. **a** Cross-sectional backscatter SEM of the early, middle, and mature stage of nacre growth shows ordering through reduced variation in the interface curvature and tablet thickness. Fourier transforms (right) of nacre (left) imaged by BSE-SEM show that angular broadening decreases from $\pm 15^\circ$ to $\pm 5^\circ$. **b** Pair-correlation functions of nacreous layers represent the probability of finding tablets spaced a given number of unit cells apart. Sharpening of peaks in later nacre indicates increasing long-range order. **c** Correlation of the thickness of tablets with nearest neighbors shows a negative correlation. If one tablet is thick, the next one tends to be thin. **d** Cumulative disorder in nacre described by a real paracrystalline model, demonstrating that the nacre mesocrystal has order between that of a crystal and a paracrystal.

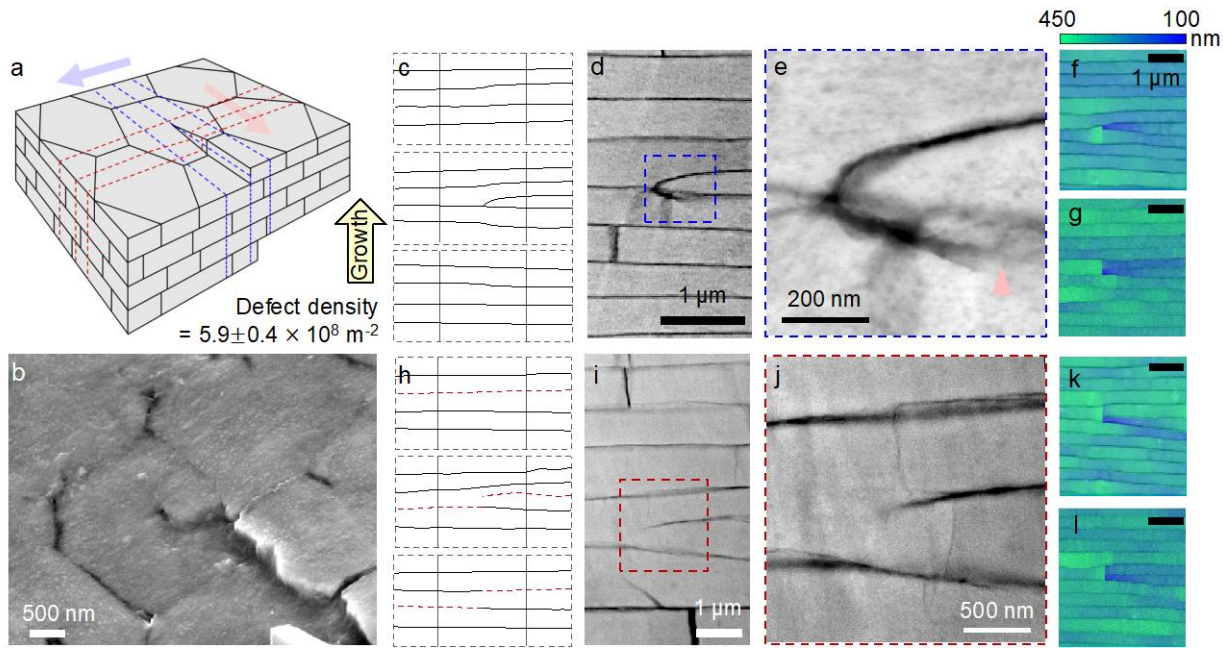


Figure 3 Topological defects in nacre. **a** Schematic of topological defects (i.e. screw dislocations) in nacre. **b** 45° tilted backscatter electron microscopy showing defect. **c** Cross-section of the schematic perpendicular to the slip plane (along the direction of blue arrow in a). **d, e** ADF STEM showing the extra tablet generated due to the defect and the mineral bridge connected to the adjacent layer. **f, g** Thickness map of the extra tablet showing abrupt change of thickness at the point of defect. **h** Cross-section of the schematic along the slip plane (along the direction of red arrow in a). **i, j** ADF STEM showing the extra organic interface split by the defect. **k, l** Thickness map of the extra organic interface showing abrupt change of thickness at the point of defect.

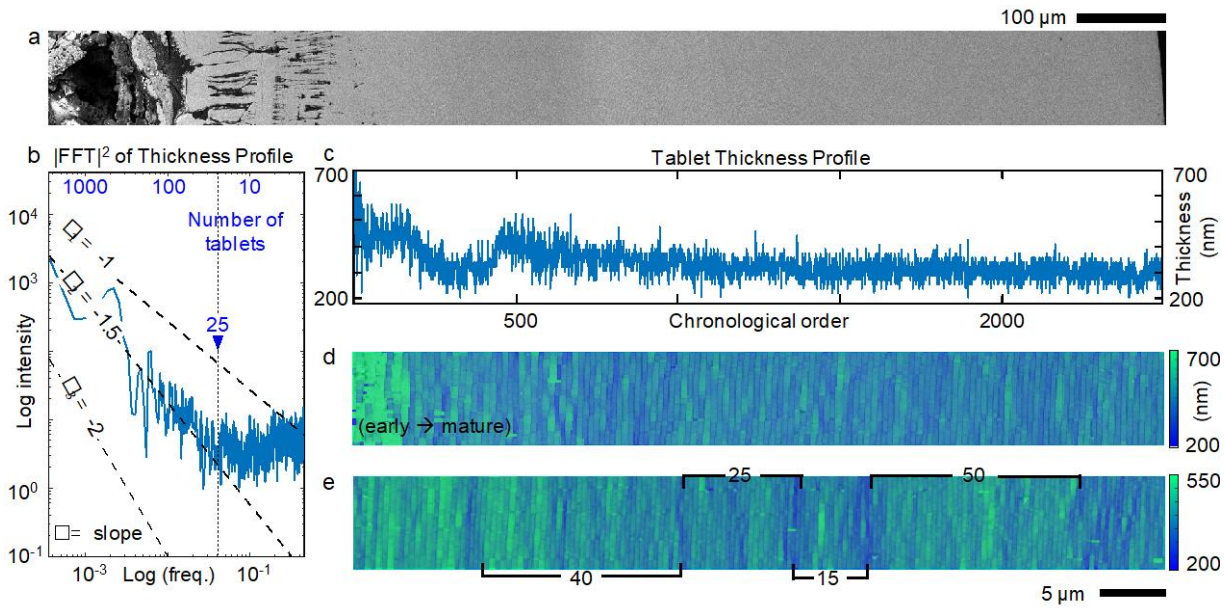


Figure 4 Growth processes of nacre throughout the entire cross-section of the pearl. **a** Overview of the pearl cross-section spanning from center to edge. **b** Log-log plot of the spectral density of the tablet thickness profile showing nacre thickness variation described by Markov processes. **c** Thickness profile across the entire pearl cross-section. **d** Thickness map from early to mature stage of nacre corresponding to early nacre. It shows an abrupt attenuation of disorder in thickness and interface curvature. **e** Thickness map of the mature nacre showing different length scales associated with tablet thickness fluctuations.

Reference

- 1 Blake, J. M. Brick (José Cornejo Franco Library, Guadalajara, Maxico, 2007).
- 2 Bellini, T., Radzihovsky, L., Toner, J. & Clark, N. A. Universality and Scaling in the Disordering of a Smectic Liquid Crystal. *Science* **294**, 1074-1079, doi:10.1126/science.1057480 (2001).
- 3 Keen, D. A. & Goodwin, A. L. The crystallography of correlated disorder. *Nature* **521**, 303-309, doi:10.1038/nature14453 (2015).
- 4 Hosemann, R., Vogel, W., Weick, D. & Baltá-Calleja, F. J. Novel aspects of the real paracrystal. *Acta Crystallographica Section A: Crystal Physics, Diffraction, Theoretical and General Crystallography* **37**, 85-91, doi:10.1107/S0567739481000156 (1981).
- 5 Wilson, J. S. Stability of Structures. *Nature* **136**, 568-571, doi:10.1038/136568a0 (1935).
- 6 Hendry, A. W. in *Structural Masonry* (ed Arnold W. Hendry) 1-15 (Macmillan Education UK, 1998).
- 7 Mark, R. & Hutchinson, P. On the Structure of the Roman Pantheon. *The Art Bulletin* **68**, 24-34, doi:10.1080/00043079.1986.10788309 (1986).
- 8 Whitesides, G. M. & Grzybowski, B. Self-Assembly at All Scales. *Science* **295**, 2418-2421, doi:10.1126/science.1070821 (2002).
- 9 Bayerlein, B. *et al.* Self-similar mesostructure evolution of the growing mollusc shell reminiscent of thermodynamically driven grain growth. *Nature Materials* **13**, 1102-1107, doi:10.1038/nmat4110 (2014).
- 10 Hovden, R. *et al.* Nanoscale assembly processes revealed in the nacreopristmatic transition zone of *Pinna nobilis* mollusc shells. *Nature Communications* **6**, 10097, doi:10.1038/ncomms10097 (2015).
- 11 Zhou, G.-T., Yao, Q.-Z., Ni, J. & Jin, G. Formation of aragonite mesocrystals and implication for biomineralization. *American Mineralogist* **94**, 293-302, doi:10.2138/am.2009.2957 (2009).
- 12 Addadi, L. & Weiner, S. A pavement of pearl. *Nature* **389**, 912-913, doi:10.1038/40010 (1997).
- 13 Gilbert, P. U. P. A. *et al.* Nacre tablet thickness records formation temperature in modern and fossil shells. *Earth and Planetary Science Letters* **460**, 281-292, doi:10.1016/j.epsl.2016.11.012 (2017).
- 14 Olson, I. C., Kozdon, R., Valley, J. W. & Gilbert, P. U. P. A. Mollusk Shell Nacre Ultrastructure Correlates with Environmental Temperature and Pressure. *Journal of the American Chemical Society* **134**, 7351-7358, doi:10.1021/ja210808s (2012).
- 15 Salman, J. *et al.* Hyperspectral interference tomography of nacre. *arXiv:2010.08170 [physics]* (2020).
- 16 Barthelat, F., Tang, H., Zavattieri, P., Li, C. & Espinosa, H. On the mechanics of mother-of-pearl: A key feature in the material hierarchical structure. *Journal of the Mechanics and Physics of Solids* **55**, 306-337, doi:10.1016/j.jmps.2006.07.007 (2007).
- 17 Gim, J. *et al.* Nanoscale deformation mechanics reveal resilience in nacre of *Pinna nobilis* shell. *Nature Communications* **10**, 4822, doi:10.1038/s41467-019-12743-z (2019).
- 18 Espinosa, H. D., Rim, J. E., Barthelat, F. & Buehler, M. J. Merger of structure and material in nacre and bone – Perspectives on de novo biomimetic materials. *Progress in Materials Science* **54**, 1059-1100, doi:10.1016/j.pmatsci.2009.05.001 (2009).

- 19 Barthelat, F., Yin, Z. & Buehler, M. J. Structure and mechanics of interfaces in biological materials. *Nature Reviews Materials* **1**, 1-16, doi:10.1038/natrevmats.2016.7 (2016).
- 20 Wegst, U. G. K., Bai, H., Saiz, E., Tomsia, A. P. & Ritchie, R. O. Bioinspired structural materials. *Nature Materials* **14**, 23-36, doi:10.1038/nmat4089 (2015).
- 21 Deng, Z. *et al.* Strategies for simultaneous strengthening and toughening via nanoscopic intracrystalline defects in a biogenic ceramic. *Nature Communications* **11**, 5678, doi:10.1038/s41467-020-19416-2 (2020).
- 22 Munch, E. *et al.* Tough, Bio-Inspired Hybrid Materials. *Science* **322**, 1516-1520, doi:10.1126/science.1164865 (2008).
- 23 Bouville, F. *et al.* Strong, tough and stiff bioinspired ceramics from brittle constituents. *Nature Materials* **13**, 508-514, doi:10.1038/nmat3915 (2014).
- 24 Zhao, C. *et al.* Layered nanocomposites by shear-flow-induced alignment of nanosheets. *Nature* **580**, 210-215, doi:10.1038/s41586-020-2161-8 (2020).
- 25 Beliaev, M., Zöllner, D., Pacureanu, A., Zaslansky, P. & Zlotnikov, I. Dynamics of topological defects and structural synchronization in a forming periodic tissue. *Nature Physics*, 1-6, doi:10.1038/s41567-020-01069-z (2021).
- 26 Jacob, D. E. *et al.* Nanostructure, composition and mechanisms of bivalve shell growth. *Geochimica et Cosmochimica Acta* **72**, 5401-5415, doi:10.1016/j.gca.2008.08.019 (2008).
- 27 Otter, L. M., Wehrmeister, U., Enzmann, F., Wolf, M. & Jacob, D. E. A Look Inside a Remarkably Large Beaded South Sea Cultured Pearl. *Gems & Gemology* **50**, 58-62, doi:10.5741/GEMS.50.1.58 (2014).
- 28 Krzemnicki, M., Friess, D., Chalus, P., Hänni, H. & Karampelas, S. X-Ray Computed Microtomography: Distinguishing Natural Pearls from Beaded and Non-Beaded Cultured Pearls. *Gems and Gemology* **46**, 128, doi:10.5741/GEMS.46.2.128 (2010).
- 29 Otter, L. M., Oluwatooshin, B. A. A., Huong, L. T.-T., Hager, T. & Jacob, D. E. Akoya Cultured Pearl Farming in Eastern Australia | Gems & Gemology. *Gem & Gemology* **53** (2017).
- 30 Checa, A. G. Physical and Biological Determinants of the Fabrication of Molluscan Shell Microstructures. *Frontiers in Marine Science* **5**, doi:10.3389/fmars.2018.00353 (2018).
- 31 Meyers, M. A. *et al.* The role of organic intertile layer in abalone nacre. *Materials Science and Engineering: C* **29**, 2398-2410, doi:10.1016/j.msec.2009.07.005 (2009).
- 32 De Yoreo, J. J. *et al.* Crystallization by particle attachment in synthetic, biogenic, and geologic environments. *Science* **349**, aaa6760-aaa6760, doi:10.1126/science.aaa6760 (2015).
- 33 Gal, A. *et al.* Particle Accretion Mechanism Underlies Biological Crystal Growth from an Amorphous Precursor Phase. *Advanced Functional Materials* **24**, 5420-5426, doi:10.1002/adfm.201400676 (2014).
- 34 Schoeppler, V. *et al.* Crystal growth kinetics as an architectural constraint on the evolution of molluscan shells. *Proceedings of the National Academy of Sciences* **116**, 20388-20397, doi:10.1073/pnas.1907229116 (2019).
- 35 Willinger, M. G., Checa, A. G., Bonarski, J. T., Faryna, M. & Berent, K. Biogenic Crystallographically Continuous Aragonite Helices: The Microstructure of the Planktonic Gastropod *Cuvierina*. *Advanced Functional Materials* **26**, 553-561, doi:<https://doi.org/10.1002/adfm.201504034> (2016).

- 36 Freer, A., Greenwood, D., Chung, P., Pannell, C. L. & Cusack, M. Aragonite Prism–Nacre Interface in Freshwater Mussels *Anodonta anatina* (Linnaeus, 1758) and *Anodonta cygnea* (L. 1758). *Crystal Growth & Design* **10**, 344-347, doi:10.1021/cg901265x (2010).
- 37 Hovden, R. *et al.* Nanoscale assembly processes revealed in the nacropelmatic transition zone of *Pinna nobilis* mollusc shells. *Nature Communications* **6**, doi:10.1038/ncomms10097 (2015).
- 38 Voyles, P. M. *et al.* Structure and physical properties of paracrystalline atomistic models of amorphous silicon. *Journal of Applied Physics* **90**, 4437-4451, doi:10.1063/1.1407319 (2001).
- 39 Savitzky, B. H. *et al.* Propagation of Structural Disorder in Epitaxially Connected Quantum Dot Solids from Atomic to Micron Scale. *Nano Letters* **16**, 5714-5718, doi:10.1021/acs.nanolett.6b02382 (2016).
- 40 Hindle, A. M. & Hosemann, R. Microparacrystals: The intermediate stage between crystalline and amorphous. *Journal of Materials Science* **26**, 5127-5133, doi:10.1007/BF01143202 (1991).
- 41 Cartwright, J. H. E., Checa, A. G., Escribano, B. & Sainz-Díaz, C. I. Spiral and target patterns in bivalve nacre manifest a natural excitable medium from layer growth of a biological liquid crystal. *Proceedings of the National Academy of Sciences* **106**, 10499-10504, doi:10.1073/pnas.0900867106 (2009).
- 42 Wada, K. Spiral Growth of Nacre. *Nature* **211**, 1427-1427, doi:10.1038/2111427a0 (1966).
- 43 Yao, N., Epstein, A. & Akey, A. Crystal growth via spiral motion in abalone shell nacre. *Journal of Materials Research* **21**, 1939-1946, doi:10.1557/jmr.2006.0252 (2006).
- 44 Yang, N. & Lu, K. Effects of transition metals on the evolution of polymer-derived SiOC ceramics. *Carbon* **171**, 88-95, doi:10.1016/j.carbon.2020.08.072 (2021).
- 45 Ikuhara, Y. Oxide Ceramics with High Density Dislocations and Their Properties. *Materials Transactions* **50**, 1626-1632, doi:10.2320/matertrans.MF200928 (2009).
- 46 Erland, S. & Greenwood, P. E. Constructing $\$1/\{\text{ensuremath}\{\omega\}\}^{\{\text{ensuremath}\{\alpha\}\}}\$$ noise from reversible Markov chains. *Physical Review E* **76**, 031114, doi:10.1103/PhysRevE.76.031114 (2007).
- 47 Erland, S., Greenwood, P. E. & Ward, L. M. “ $1/f \upalpha$ noise” is equivalent to an eigenstructure power relation. *EPL (Europhysics Letters)* **95**, 60006, doi:10.1209/0295-5075/95/60006 (2011).
- 48 Bak, P., Tang, C. & Wiesenfeld, K. Self-organized criticality: An explanation of the $1/f$ noise. *Physical Review Letters* **59**, 381-384, doi:10.1103/PhysRevLett.59.381 (1987).
- 49 Bak, P., Tang, C. & Wiesenfeld, K. Self-organized criticality. *Physical Review A* **38**, 364-374, doi:10.1103/PhysRevA.38.364 (1988).
- 50 Cajochen, C. *et al.* Evidence that the Lunar Cycle Influences Human Sleep. *Current Biology* **23**, 1485-1488, doi:10.1016/j.cub.2013.06.029 (2013).
- 51 Tran, D. *et al.* Field Chronobiology of a Molluscan Bivalve: How the Moon and Sun Cycles Interact to Drive Oyster Activity Rhythms. *Chronobiology International* **28**, 307-317, doi:10.3109/07420528.2011.565897 (2011).
- 52 Nakajima, M. *et al.* Reconstitution of Circadian Oscillation of Cyanobacterial KaiC Phosphorylation in Vitro. *Science* **308**, 414-415, doi:10.1126/science.1108451 (2005).
- 53 Scott, M., Gunderson, C. W., Mateescu, E. M., Zhang, Z. & Hwa, T. Interdependence of Cell Growth and Gene Expression: Origins and Consequences. *Science* **330**, 1099-1102, doi:10.1126/science.1192588 (2010).

- 54 Zhang, L. *et al.* Dissociation of Circadian and Circatidal Timekeeping in the Marine Crustacean *Eurydice pulchra*. *Current Biology* **23**, 1863-1873, doi:10.1016/j.cub.2013.08.038 (2013).
- 55 Tu, B. P. & McKnight, S. L. Metabolic cycles as an underlying basis of biological oscillations. *Nature Reviews Molecular Cell Biology* **7**, 696-701, doi:10.1038/nrm1980 (2006).
- 56 Carey, H. V., Andrews, M. T. & Martin, S. L. Mammalian Hibernation: Cellular and Molecular Responses to Depressed Metabolism and Low Temperature. *Physiological Reviews* **83**, 1153-1181, doi:10.1152/physrev.00008.2003 (2003).
- 57 Storey, K. B. & Storey, J. M. Aestivation: signaling and hypometabolism. *Journal of Experimental Biology* **215**, 1425-1433, doi:10.1242/jeb.054403 (2012).
- 58 Withers, P., Pedler, S. & Guppy, M. Physiological Adjustments during Aestivation by the Australian Land Snail *Rhagada tescorum* (Mollusca : Pulmonata : Camaenidae). *Australian Journal of Zoology* **45**, 599-611, doi:10.1071/z097009 (1997).
- 59 van der Weijden, A., Winkens, M., Schoenmakers, S. M. C., Huck, W. T. S. & Korevaar, P. A. Autonomous mesoscale positioning emerging from myelin filament self-organization and Marangoni flows. *Nature Communications* **11**, 4800, doi:10.1038/s41467-020-18555-w (2020).
- 60 Karsenti, E. Self-organization in cell biology: a brief history. *Nature Reviews Molecular Cell Biology* **9**, 255-262, doi:10.1038/nrm2357 (2008).
- 61 te Brinke, E. *et al.* Dissipative adaptation in driven self-assembly leading to self-dividing fibrils. *Nature Nanotechnology* **13**, 849-855, doi:10.1038/s41565-018-0192-1 (2018).
- 62 Liu, M., Li, Q. & Zhu, F. Threshold negative binomial autoregressive model. *Statistics* **53**, 1-25, doi:10.1080/02331888.2018.1546307 (2019).
- 63 Qiu, F., Sridharan, H. & Chun, Y. Spatial Autoregressive Model for Population Estimation at the Census Block Level Using LIDAR-derived Building Volume Information. *Cartography and Geographic Information Science* **37**, 239-257, doi:10.1559/152304010792194949 (2010).
- 64 Hayes, R. J. Methods for assessing whether change depends on initial value. *Statistics in Medicine* **7**, 915-927, doi:<https://doi.org/10.1002/sim.4780070903> (1988).
- 65 Hänni, H. A. A short review of the use of ‘keshi’ as a term to describe pearls. *The Journal of Gemmology* **30**, 51-58, doi:10.15506/JoG.2006.30.1.51 (2006).
- 66 Nudelman, F. Nacre biomineralisation: A review on the mechanisms of crystal nucleation. *Seminars in Cell & Developmental Biology* **46**, 2-10, doi:10.1016/j.semcdb.2015.07.004 (2015).
- 67 Lin, A. & Meyers, M. A. Growth and structure in abalone shell. *Materials Science and Engineering: A* **390**, 27-41, doi:10.1016/j.msea.2004.06.072 (2005).
- 68 Runnegar, B. in *Origin, Evolution, and Modern Aspects of Biomineralization in Plants and Animals* (ed Rex E. Crick) 75-94 (Springer US, 1989).
- 69 Schwartz, J. *et al.* Removing Stripes, Scratches, and Curtaining with Nonrecoverable Compressed Sensing. *Microscopy and Microanalysis* **25**, 705-710, doi:10.1017/S1431927619000254 (2019).

Figures

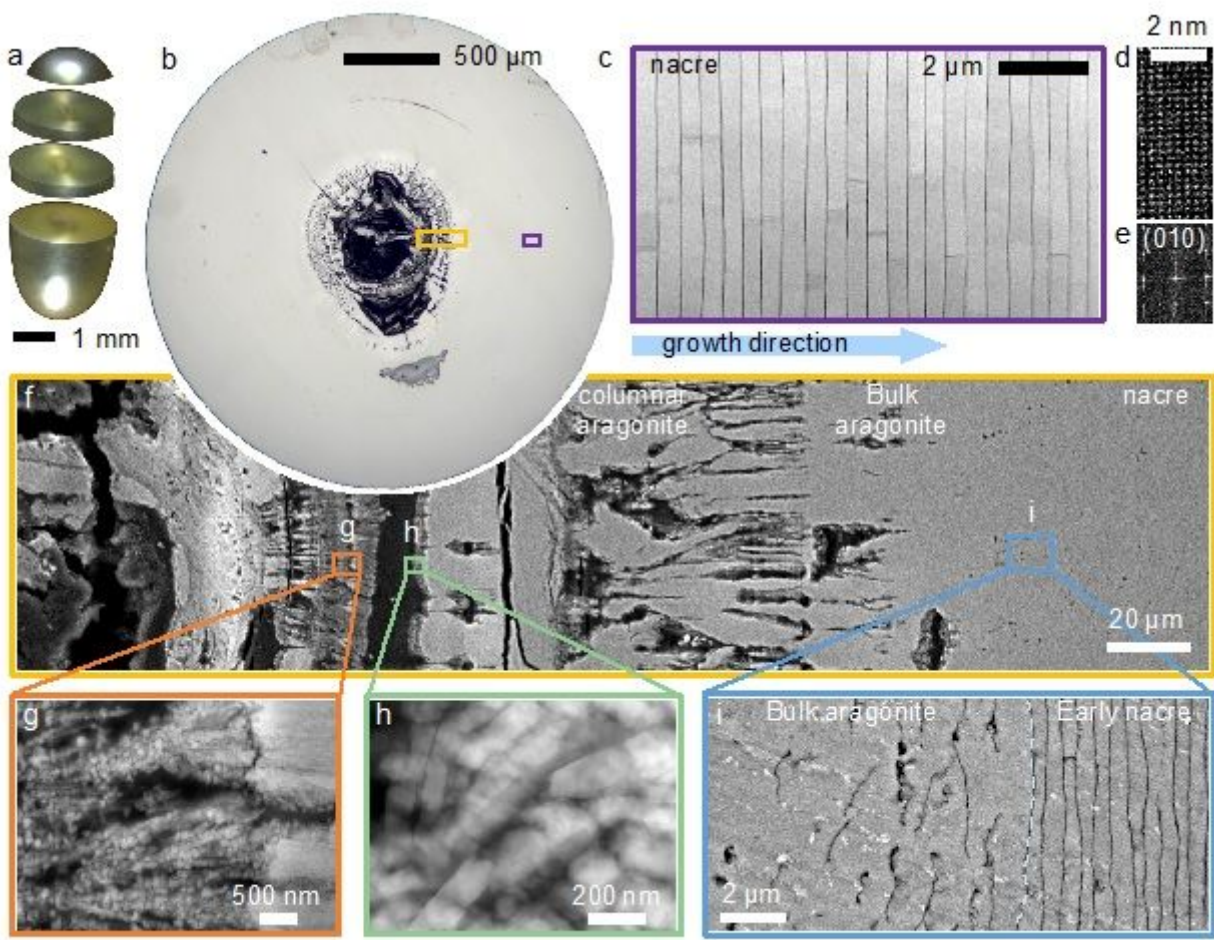


Figure 1

Formation of non-bead-cultured akoya "keshi" pearls produced in a *Pinctada imbricata fucata* mollusk. a Optical overview of a non-beaded keshi cultured pearl showing iridescence due to the interplay of constructive interference at nacre tablet layers with light. b Cross-section showing CaCO₃ growth begins onto an organic center. c Mature nacre (purple box in b) showing ordered state in their thickness and interface curvature. d,e Atomic resolution ADF STEM of mature nacre and its corresponding Fourier Transform indicating highly crystalline nacre and a lattice constant that is consistent with aragonite. f Cross-sectional backscatter SEM at the center of the pearl (yellow box in b) showing transition from spherulitic aragonite structures to nacre. g,h Oriented attachment of nanocrystallites that form massive, structurally indistinct aragonite structure. i Formation of nacre begins directly on massive, structurally indistinct aragonite.

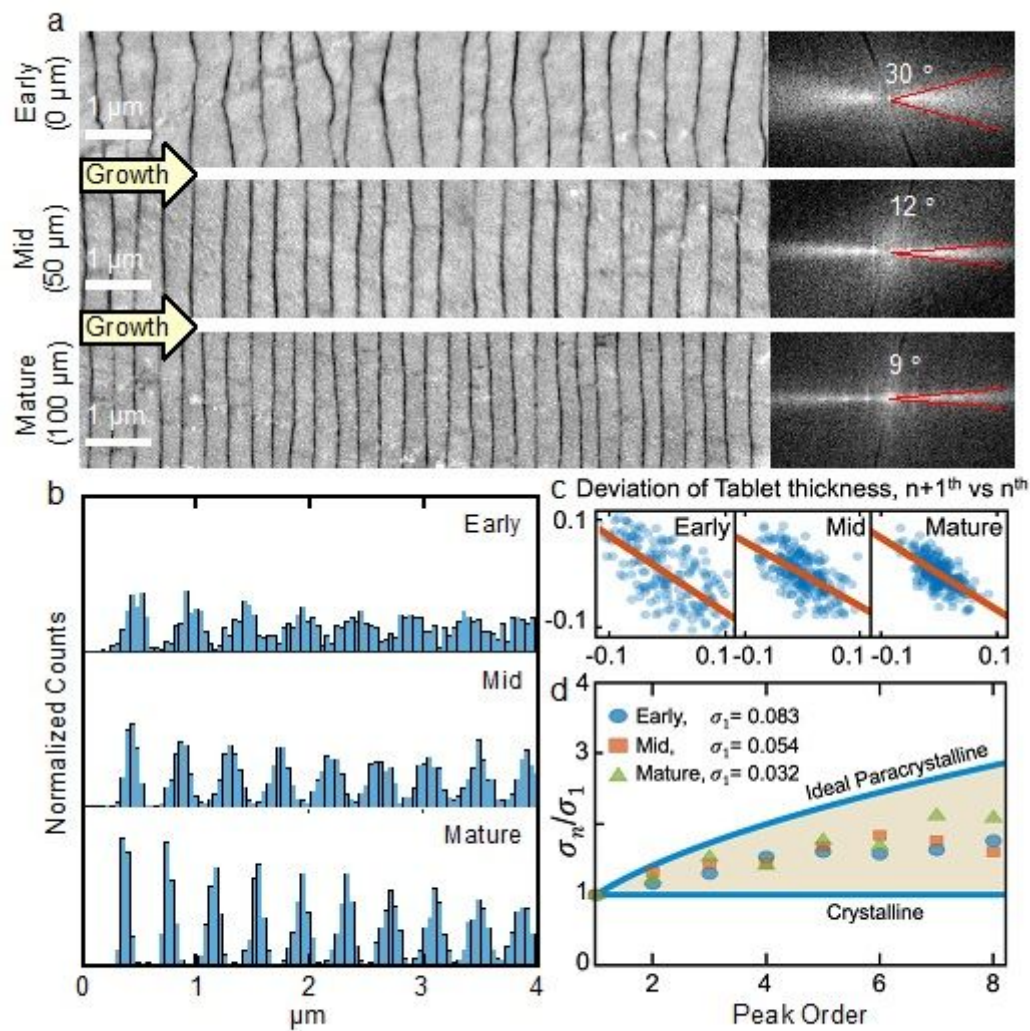


Figure 2

Quantification of mesocrystallinity in nacre. a Cross-sectional backscatter SEM of the early, middle, and mature stage of nacre growth shows ordering through reduced variation in the interface curvature and tablet thickness. Fourier transforms (right) of nacre (left) imaged by BSE-SEM show that angular broadening decreases from $\pm 15^\circ$ to $\pm 5^\circ$. b Pair-correlation functions of nacreous layers represent the probability of finding tablets spaced a given number of unit cells apart. Sharpening of peaks in later nacre indicates increasing long-range order. c Correlation of the thickness of tablets with nearest neighbors shows a negative correlation. If one tablet is thick, the next one tends to be thin. d Cumulative disorder in nacre described by a real paracrystalline model, demonstrating that the nacre mesocrystal has order between that of a crystal and a paracrystal.

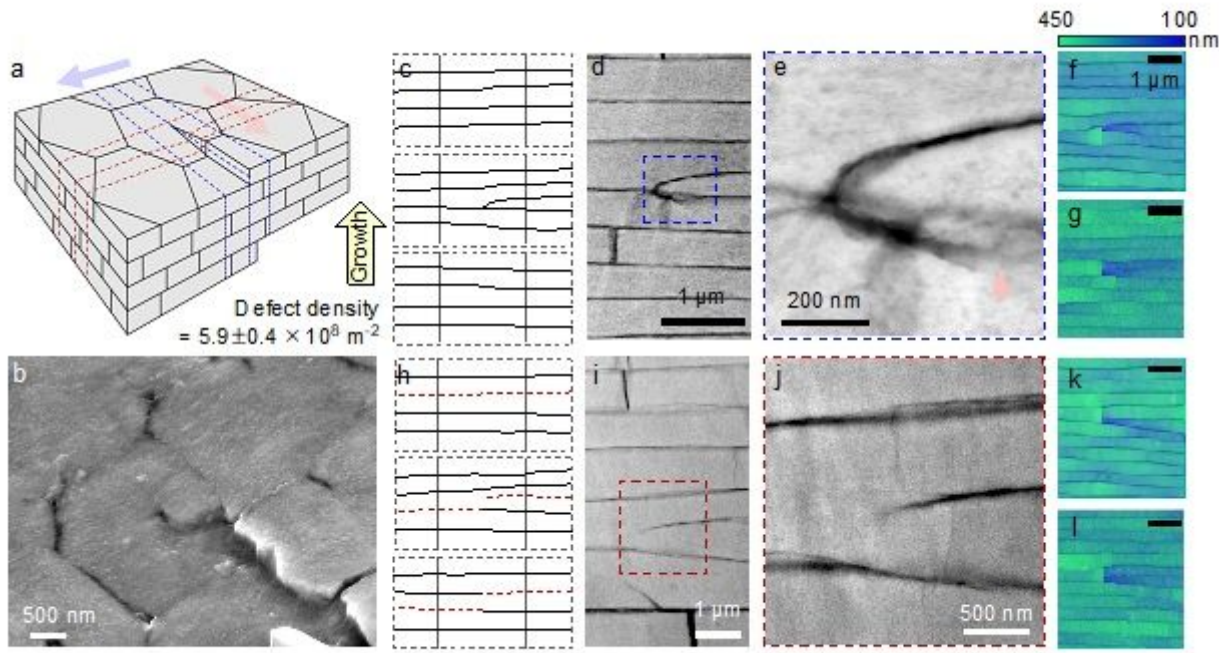


Figure 3

Topological defects in nacre. a Schematic of topological defects (i.e. screw dislocations) in nacre. b 45° tilted backscatter electron microscopy showing defect. c Cross-section of the schematic perpendicular to the slip plane (along the direction of blue arrow in a). d, e ADF STEM showing the extra tablet generated due to the defect and the mineral bridge connected to the adjacent layer. f, g Thickness map of the extra tablet showing abrupt change of thickness at the point of defect. h Cross-section of the schematic along the slip plane (along the direction of red arrow in a). i, j ADF STEM showing the extra organic interface split by the defect. k, l Thickness map of the extra organic interface showing abrupt change of thickness at the point of defect.

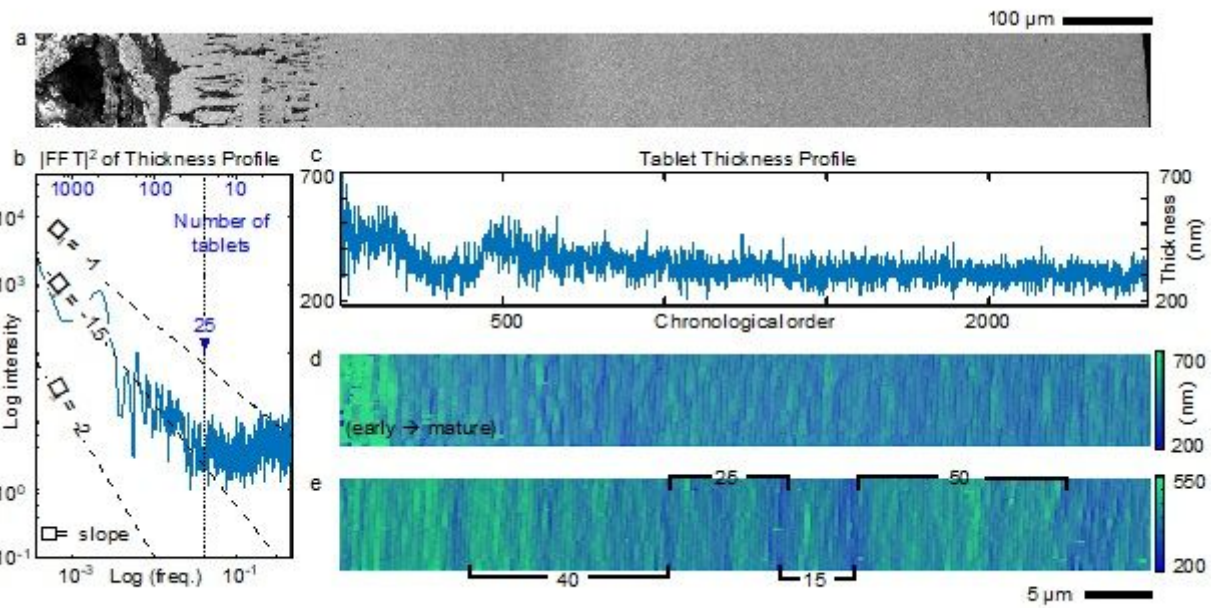


Figure 4

Growth processes of nacre throughout the entire cross-section of the pearl. a Overview of the pearl cross-section spanning from center to edge. b Log-log plot of the spectral density of the tablet thickness profile showing nacre thickness variation described by Markov processes. c Thickness profile across the entire pearl cross-section. d Thickness map from early to mature stage of nacre corresponding to early nacre. It shows an abrupt attenuation of disorder in thickness and interface curvature. e Thickness map of the mature nacre showing different length scales associated with tablet thickness fluctuations.

Supplementary Files

This is a list of supplementary files associated with this preprint. Click to download.

- [TheMesoscaleCrystallinityofNacreousPearlsSlvF.docx](#)